Article

Fractional quantum Hall phases in high-mobility n-type molybdenum disulfide transistors

Siwen Zhao [1,17], Jinqiang Huang[2,3,17], Valentin Crépel [4,17], Zhiren Xiong[5,6], Xingguang Wu[5,6], Tongyao Zhang [5,6], Hanwen Wang[1], Xiangyan Han[7], Zhengyu Li[8], Chuanying Xi[8], Senyang Pan [8], Zhaosheng Wang[8], Guangli Kuang[8], Jun Luo[9], Qinxin Shen[9,10], Jie Yang[9], Rui Zhou [9], Kenji Watanabe [11], Takashi Taniguchi [12], Benjamin Sacépé [13], Jing Zhang [5,6] ✉, Ning Wang [14], Jianming Lu [7] ✉, Nicolas Regnault [15,16] ✉ & Zheng Vitto Han [1,5,6] ✉

Transistors based on semiconducting transition metal dichalcogenides can, in theory, offer high carrier mobilities, strong spin–orbit coupling and inherently strong electronic interactions at the quantum ground states. This makes them well suited for use in nanoelectronics at low temperatures. However, creating robust ohmic contacts to transition metal dichalcogenide layers at cryogenic temperatures is difficult. As a result, it is not possible to reach the quantum limit at which the Fermi level is close to the band edge and thus probe electron correlations in the fractionally filled Landau-level regime. Here we show that ohmic contacts to n-type molybdenum disulfide can be created over a temperature range from millikelvins to 300 K using a window-contacted technique. We observe field-effect mobilities of over 100,000 cm^2 V^{-1} s^{-1} and quantum mobilities of over 3,000 cm^2 V^{-1} s^{-1} in the conduction band at low temperatures. We also report evidence for fractional quantum Hall states at filling fractions of 4/5 and 2/5 in the lowest Landau levels of bilayer molybdenum disulfide.

At low temperatures, transition metal dichalcogenide (TMD) transistors can potentially offer high mobilities, strong spin–orbit coupling and large effective masses. They could, therefore, be used to explore various electronic interactions. One such interaction-driven phenomena is the fractional quantum Hall (FQH) state—the many-body effects of incompressible gaps at partial fillings of Landau levels (LLs)[1–4]. FQH states are revealed through their edge conduction channels, whose transport exhibits a minimum of longitudinal resistivity ρ_{xx} and a transverse conductivity σ_{xy} quantized as $\nu e^2/h$, where e is the elementary charge and h is Planck's constant. In the composite fermion theory[5–7], the main series of fractions is given by

$\nu = p/(2kp + 1)$ (k and p are integers) or its particle–hole (p-h) conjugate partner ($\nu = 1 - p/(2kp + 1)$).

The FQH states are considered of potential use in topological quantum computations due to the non-conventional exchange statistics in the non-Abelian 5/2 states that have been observed in GaAs and ZnO semiconductors[8–10]. Theoretical efforts have also been focused on the development of superconducting FQH hybrid systems to engineer parafermions—a generalized version of Majorana fermions—for quantum computing purposes with fractional topological orders[11–13]. However, only a handful of solid-state two-dimensional electron gas (2DEG) systems have been developed that exhibit fractionally
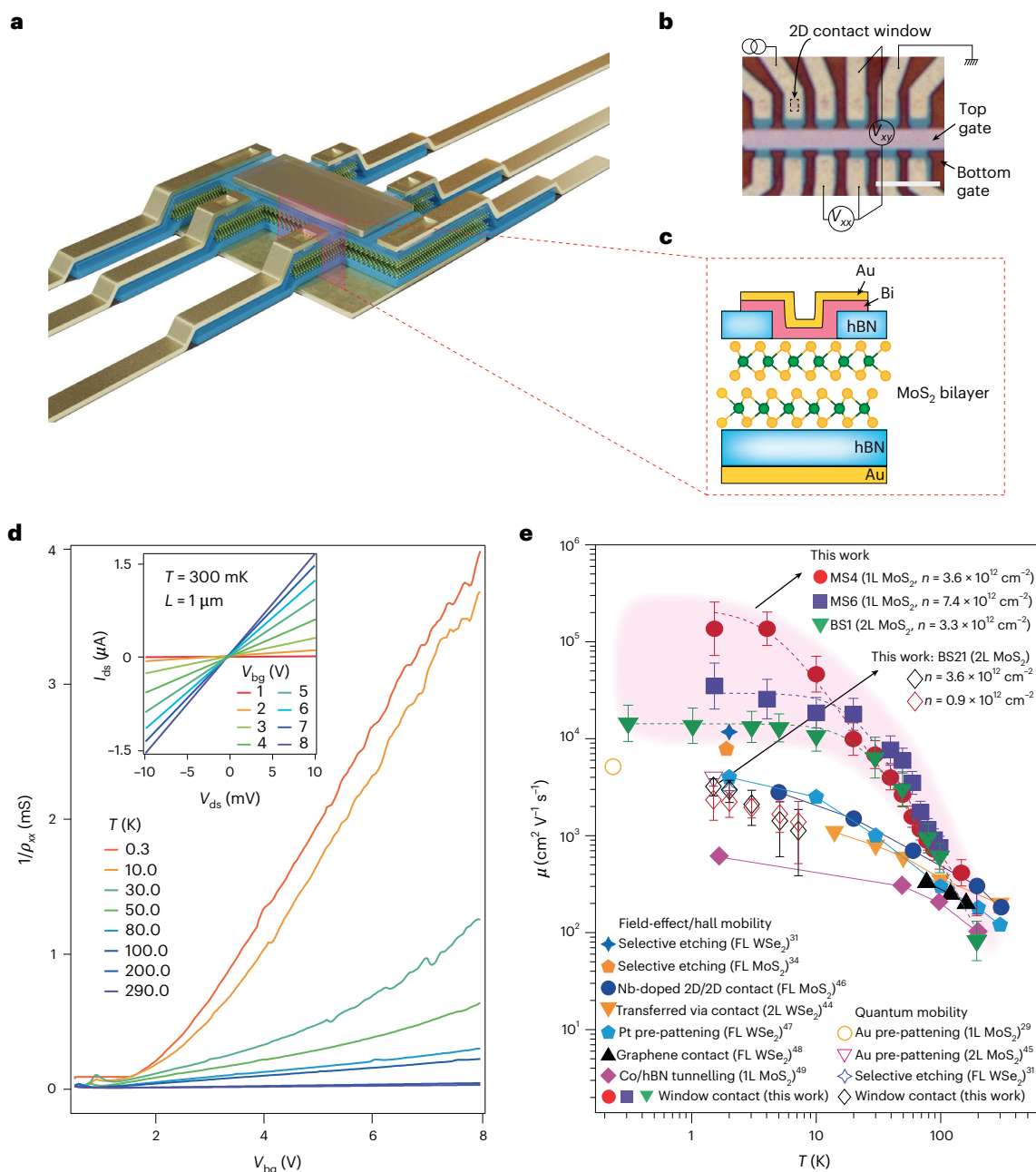
Fig. 1 | Characterizations of window-contacted MoS₂ transistors. a, Schematic of the fabricated device. **b**, Optical image of a typical dual-gated bilayer MoS₂ device. One of the 2D contact windows is highlighted by black dashed lines. Scale bar, 5 μm. **c**, Artistic view of the cross-section at the contact (indicated by the purple window in **a**) of the device under investigation. Bi/Au (25/30 nm) electrodes are deposited through the pre-patterned window in the top hBN. **d**, Field-effect curves (longitudinal conductivity ρ_{xx}^{-1} versus back-gate voltage V_{bg}) of sample BS1 measured at different temperatures ranging from 290 K to 300 mK. The inset shows the output characteristics at low drain–source bias obtained at $T = 300$ mK for a channel length of $L = 1$ μm for different V_{bg} values. Notice that the output curves are linear, which is a characteristic of an ohmic contact. **e**, Summarization of state-of-the-art charge mobilities obtained in TMDs. Field-effect electron mobility in MoS₂ obtained in this work is one of the highest among TMD transistors with different layers (1L, 2L and FL represent one

layer, two layers and few layers, respectively) using different contact methods. The solid symbols represent the field-effect mobility, and the hollow symbols represent the quantum mobility in various TMD systems reported (Supplementary Figs. 6 and 7). The values of field-effect mobility at certain carrier densities n in our monolayer samples named MS4 and MS6 and bilayer sample named BS1 are plotted in the shaded region, with the arrow pointing to it. The shaded region and the solid lines connecting the data points serve as guides for the eyes. The dashed lines are the fitting curves obtained by applying Matthiessen's rule for the temperature dependence of a semiconductor, written as $\frac{1}{\mu(T)} = \frac{1}{\mu_{imp}} + \frac{1}{\mu_{ph}(T)}$, where μ_{imp} is the Coulomb impurity-limited mobility at low temperatures and μ_{ph} is the one affected by optical phonons[64]. The fitting errors are propagated and indicated by the error bars.

quantized σ_{xy} plateaus, including semiconductor quantum wells[14–16] and graphene[17–22]. The SU(4) symmetry breaking of LLs in graphene has, for instance, led to collective states including denominator FQH states in the lowest LLs and in higher LLs[23–27].

Semiconducting TMDs have a variety of interacting phases due to the massive Dirac fermions character of their charge carriers and their spin–orbit coupling[28–30]. Recently, mono- or few-layered semiconducting TMDs have been shown to exhibit giant effective g-factors (here g-factor

Table 1 | Summary of the characteristics of typical samples

Sample ID	Layer number	Channel length (µm)	Channel width (µm)	Field-effect/Hall mobility at 1.5 K ($cm^2 V^{-1} s^{-1}$)	Quantum mobility at 1.5 K ($cm^2 V^{-1} s^{-1}$)
BS1	2	1.5	1.5	13,736 ($n = 3.3 \times 10^{12} cm^{-2}$)	2,220 ($n = 0.7 \times 10^{12} cm^{-2}$)
BS12	2	1.5	1.5	N/A	2,273 ($n = 6.4 \times 10^{12} cm^{-2}$)
BS14	2	1.5	1.5	26,914 ($n = 2.15 \times 10^{12} cm^{-2}$)	2,702 ($n = 4.2 \times 10^{12} cm^{-2}$)
BS16	2	1.5	1.5	N/A	3,390 ($n = 7.1 \times 10^{12} cm^{-2}$)
BS18	2	1.5	1.5	N/A	1,724 ($n = 9.0 \times 10^{12} cm^{-2}$)
BS21	2	1.5	1.5	16,447 ($n = 4 \times 10^{12} cm^{-2}$)	3,260 ($n = 3.6 \times 10^{12} cm^{-2}$)
MS4	1	1.5	1.5	116,691 ($n = 3.6 \times 10^{12} cm^{-2}$)	N/A
MS6	1	1.5	1.5	35,294 ($n = 7.4 \times 10^{12} cm^{-2}$)	N/A

is a dimensionless quantity that characterizes the magnetic moment and angular momentum of a particle)[30–33], non-conventional sequence of Hall plateaus[34,35] and LL crossings with possible quantum Hall antiferromagnetic phases[36]. However, most of these studies were performed far above the quantum limit and at filling fractions ν larger than 1.

Capacitance probes on high-quality monolayer tungsten diselenide (WSe₂) has revealed a series of FQH gaps in the lowest and first excited LLs[37], suggesting that fractional quantizations are, in principle, available in TMDs for transport measurements—a requirement for the construction of quantum devices based on FQH states. Still, FQH plateaus in TMDs—particularly in the lowest LLs at which electron interactions are the most pronounced—remain elusive. The challenge lies in the lack of access to low carrier density close to the band edge, an ohmic contact to the semiconducting channel at low temperature and an appropriate dielectric environment that favours the Coulomb interaction.

In this Article, we show that a window-contacted technique can create ohmic contacts to n-type molybdenum disulfide (MoS₂) over a temperature range from millikelvins to 300 K. We observe high field-effect electron mobilities (exceeding 100,000 $cm^2 V^{-1} s^{-1}$) and quantum mobilities (over 3,000 $cm^2 V^{-1} s^{-1}$) at low temperatures. We probe the electrical transport of monolayer MoS₂ down to the low carrier density required to reach the quantum limit. We report evidence for FQH at filling fractions of 4/5 and 2/5 in bilayer MoS₂ via transport measurements under high magnetic fields of up to 34 T and a base temperature of 300 mK. Our calculations and measurements suggest that under the application of a finite vertical electric field (E_z), the system behaves like a monolayer MoS₂ for which the first four (lowest and first excited) LLs in the conduction band are layer-valley locked, and the spin degeneracy is fully lifted by the Zeeman energy. Therefore, the LL spectra of the MoS₂ bilayer, together with the asymmetric ohmic contact to the high-mobility bilayer semiconducting channel, provide a model to investigate electron–electron interactions in the FQH regime.

Windowed ohmic contact to n-type MoS₂

Various methods, including phase-engineered edge contact and the use of Pt or Au bottom electrodes[29,38–40], have been used to try and establish electrical contact with semiconducting MoS₂ for quantum transport studies, but it has not been possible to probe the lowest LL approaching the quantum limit through transport measurements. Recently, low-melting-point metals like Bi and (01̄12)-faceted Sb have emerged as potential candidates for forming ohmic contacts with the MoS₂ channel[41]. However, thus far, these studies have been limited to relatively high-temperature regimes (above a few tens of kelvins). Here we adopt the Bi contact method[42], but modify it into a two-dimensional (2D) windowed convention.

We first pre-pattern etched-through windows (with sizes of ~1 × 1 µm²) in few-layered hexagonal boron nitride (hBN), which are further used as a top boron nitride for encapsulating mono- or bilayer MoS₂. hBN/MoS₂/hBN sandwiches are fabricated in a nitrogen-filled

glove box using the dry-transfer method[43]. The workflow of our sample fabrication process is illustrated in Supplementary Fig. 1, with several typical samples shown in Supplementary Fig. 2. Figure 1a shows an artistic view of the fabricated device. Thermal evaporation of Bi/Au (25/30 nm) is carried out after lithography that exposes the 2D window opened in the top hBN. As shown in the optical image of a typical device (Fig. 1b), the 2D-windowed contact (Fig. 1b, dashed box) is visible for each electrical lead. The device is equipped with top and bottom gates, and etch shaped into Hall bars for electrical measurements (the Methods provides more details).

Figure 1c depicts a schematic of the windowed Bi contact on bilayer MoS₂, providing a cross-sectional view of the shaded section shown in Fig. 1a. Clearly, the top surface of MoS₂ is contacted by Bi/Au in a 2D manner, which enables the formation of an ohmic contact to the conduction electrons in semiconducting MoS₂ down to the base temperature of sub-1 K. As discussed in Supplementary Fig. 3, by applying the transfer length method, the contact resistivity in our devices is estimated to be about 450 Ω µm at T = 1.5 K. In the typical dual-gated samples, the contact areas are doped by only the bottom gate (Fig. 1a,b). Taking sample BS21 as an example, the contact resistance is estimated to be a few hundred ohms by subtracting the four-probe resistance from the two-probe resistance at 1.5 K (Supplementary Fig. 4). Such a contact resistance is sufficiently low to perform quantum transport measurements in the quantum Hall regime. As shown in Supplementary Fig. 4, the contact resistance is maintained below 10 kΩ µm with a carrier density reaching as low as ~2 × 10¹¹ cm⁻². This value corresponds to the critical carrier density where the metal–insulator transition takes place in the present system (Supplementary Fig. 5). Field-effect curves (longitudinal conductivity ρ_{xx}^{-1} as a function of back-gate voltage V_{bg}) recorded in a typical device BS1 at different temperatures ranging from 290 K to 300 mK are shown in Fig. 1d. Evidently, the device exhibits enhanced conductivity as the temperature decreases, and the two-terminal I–V curves remain linear at the base temperature of 300 mK (Fig. 1d, inset), suggesting an ohmic contact to the n-type semiconductor. Figure 1e showcases the state-of-the-art field-effect/Hall mobilities obtained in typical TMD transistors (n type for MoS₂ and p type for WSe₂) as a function of temperature using different contact methods[31,34,44–49]. A summary of the characteristics of the typical measured samples is listed in Table 1. The field-effect/Hall electron mobility is estimated to be 10^4–10^5 $cm^2 V^{-1} s^{-1}$ in the MoS₂ devices in our work, benchmarking some of the best performances at sub-1 K temperatures. It is, thus, worth noting that our contact method may promote future applications of high-electron-mobility transistors devices using MoS₂ as a platform, especially at cryogenic temperatures. Notice that the above-mentioned analysis is the so-called field-effect mobility (or relatively similar to Hall mobility) and an examination of the quantum mobility (defined by $1/B_{OSC}$, where B_{OSC} is the onset of quantum oscillations). More details on the measurements of Hall and quantum mobility of the current system are provided in Supplementary Figs. 6 and 7.
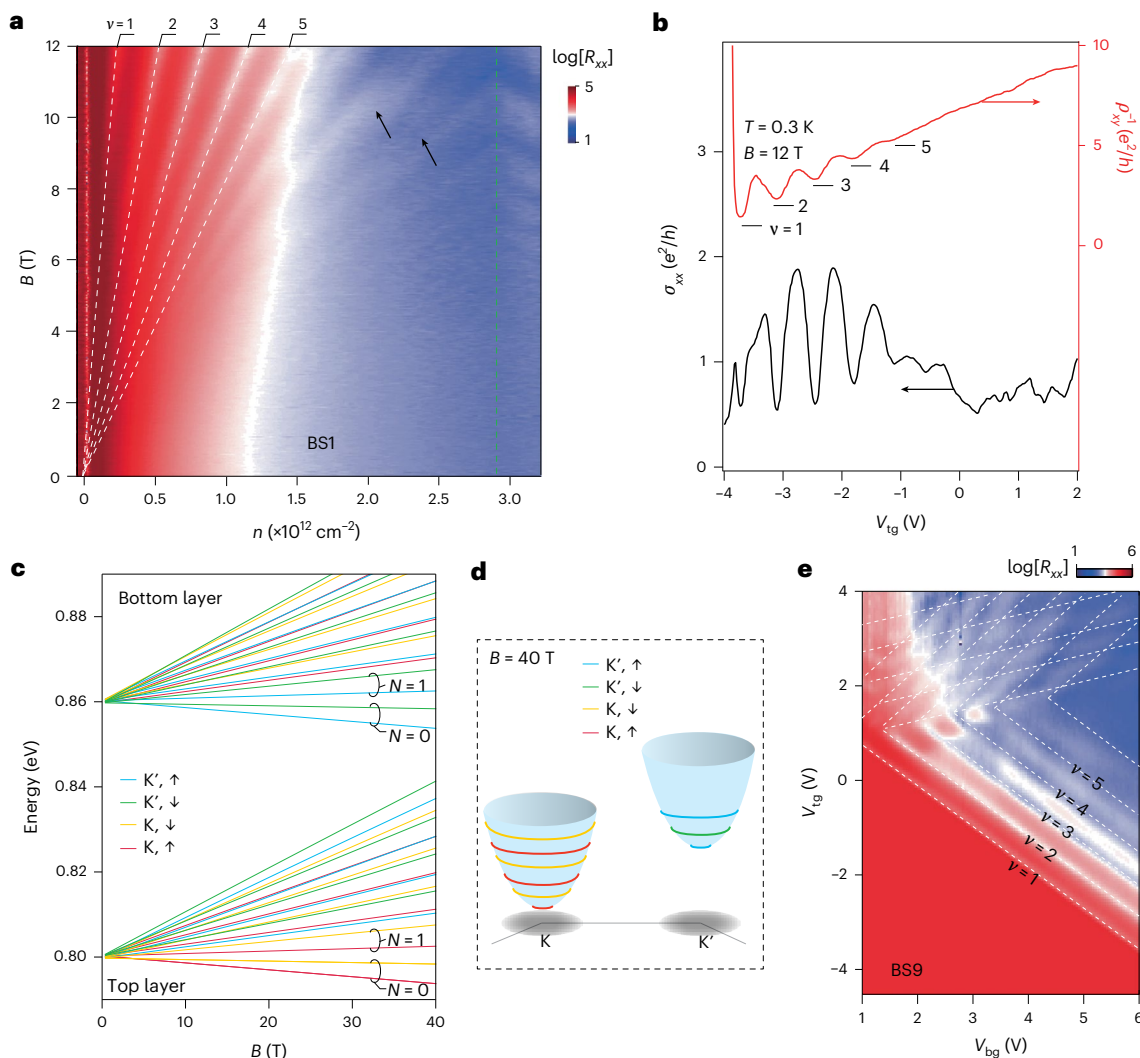
Fig. 2 | Electrical transport in bilayer MoS$_2$ in the single-particle regime.
a, Landau fan diagram (longitudinal resistance R_{xx} as a function of B and n) of sample BS1 measured at $T = 300$ mK and $V_{bg} = 4.72$ V, in the magnetic-field range from 0 T to 12 T. The white dashed lines are guides for the eyes, and their crossing point indicates the band edge. The black arrows indicate the the emergence of LL crossings from different flavours. The green dashed line marks the boundary between the two sets of LLs from the top and bottom layers. **b**, Line profile of $\sigma_{xx} = \rho_{xx}/(\rho_{xx}^2 + \rho_{xy}^2)$ and transverse conductivity ρ_{xy}^{-1} at $B = 12$ T and $T = 0.3$ K,

extracted from **a**, where σ_{xx} and ρ_{xx} represent the longitudinal conductivity and resistivity, respectively. The bottom axis corresponds to the top-gate voltages. **c**, Calculated LLs as a function of energy and magnetic field (Methods). N represents the Landau index. **d**, Cartoon illustration of the calculated several first LLs at the K and K' valleys at $B = 40$ T and $E_z = 60$ meV. For simplicity, only part of the Brillouin zone is shown. **e**, Channel resistance of an asymmetrically contacted bilayer MoS$_2$ sample BS9 as a function of V_{bg} and V_{tg}. The dashed lines are guides for the eyes.

LLs of bilayer MoS$_2$

We now study the dual-gated mapping of the channel resistance of typical MoS$_2$ devices under a finite perpendicular magnetic field B. As shown in Supplementary Fig. 8, the dual-gate field-effect colour maps at $B = 12$ T and $T = 0.3$ K are plotted into the parameter space of n and D, with total carrier density $n = (C_{tg}V_{tg} + C_{bg}V_{bg})/e - n_0$ and applied average electric displacement field $D = (C_{tg}V_{tg} - C_{bg}V_{bg})/2\epsilon_0 - D_0$, where C_{tg} and C_{bg} are the top- and bottom-gate capacitances per area, respectively. V_{tg} and V_{bg} are the top- and bottom-gate voltages, respectively. n_0 and D_0 are the residual doping and residual displacement fields, respectively. LLs close to the band edges are well developed for both monolayer (Supplementary Fig. 8a) and bilayer (Supplementary Fig. 8b) MoS$_2$. Landau fan scanned at a fixed $D = -0.4$ V nm^{-1} for the bilayer sample is shown in Supplementary Fig. 8c. Evidently, the lowest LL can be observed above ~7 T, with the first five LLs indexed by full-degeneracy-lifted integers v from 1 to 5. Landau fan spectra measured in the same device but at a fixed $V_{bg} = 4.72$ V is shown in Fig. 2a. Similar to that in Supplementary Fig. 8c, the first five LLs are highlighted with dashed

white lines, which extrapolate at $n \approx 0$ cm^{-2}, that is, the band edge. This extremely low carrier density available in our current system allows us to investigate the electronic states below the quantum limit of $v = 1$. A line profile of the longitudinal and transverse conductivities (defined as $\sigma_{xx} = \rho_{xx}/(\rho_{xx}^2 + \rho_{xy}^2)$ and ρ_{xy}^{-1}, where ρ_{xx} and ρ_{xy} are the longitudinal and transverse resistivities, respectively; a matrix inversion format is used for σ_{xx} to ensure better visibility due to the highly resistive ρ_{xx}; Supplementary Fig. 9) are plotted in Fig. 2b. The quantization of Hall plateaus for the first five LLs can be seen, with the conductance minima observed in their corresponding σ_{xx}. Higher filling fractions become smeared out and level crossing seems to take place as that in the doping range of $n > 1.5 \times 10^{12}$ cm^{-2} (Fig. 2a, solid black arrows). Notice that the LL crossing can be complicated in multilayered MoS$_2$, as reported previously[28,30,36], but is nevertheless captured to a large extent by our calculations (Supplementary Fig. 10). In addition, Fig. 2a displays another set of LL-like features (right side of the green dashed line), which originates from the asymmetric electrical contact to the bilayer MoS$_2$, and will be discussed later.
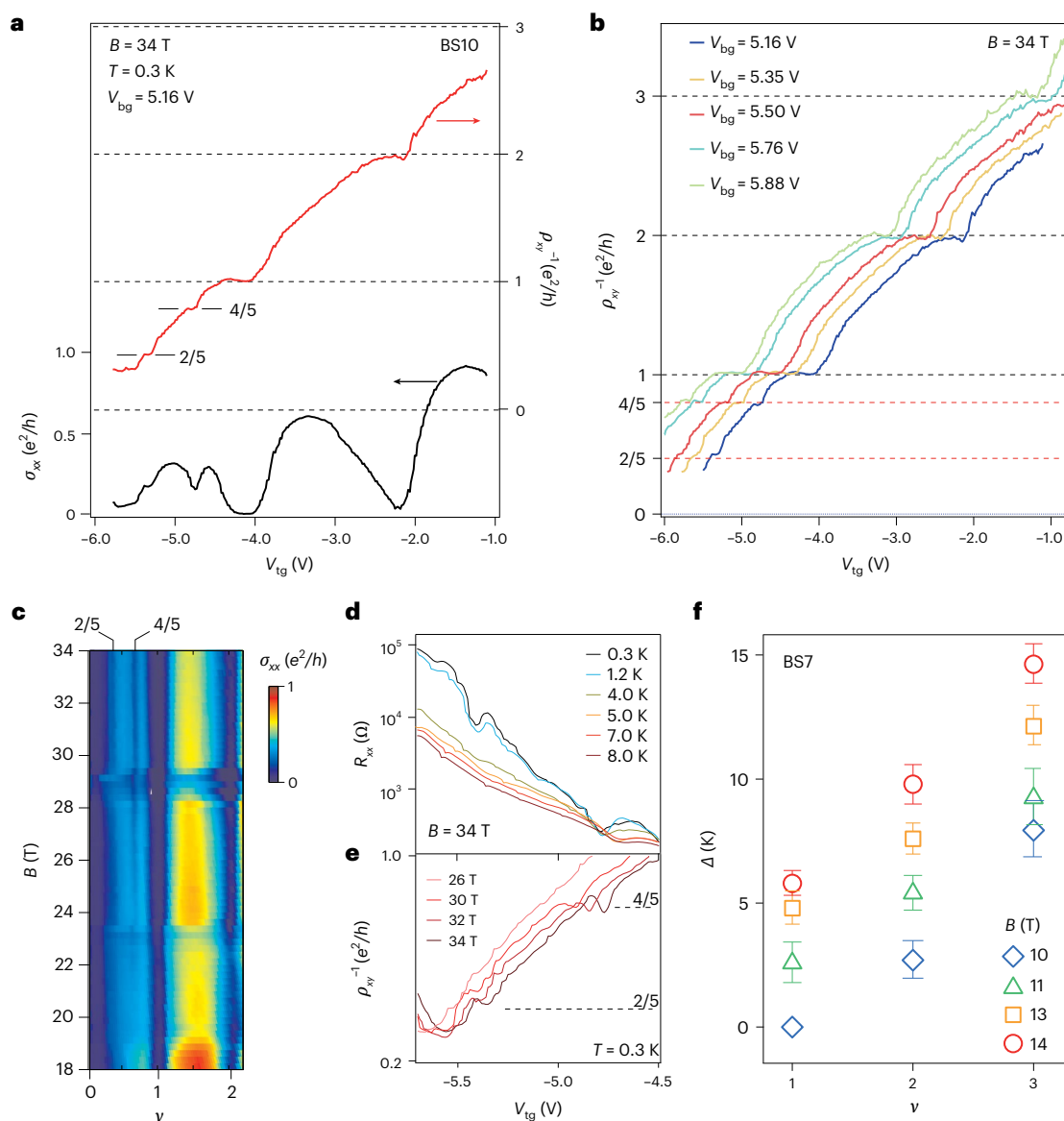
Fig. 3 | FQH states of bilayer MoS$_2$ in the lowest LL in the conduction band.
a, $\sigma_{xx} = \rho_{xx}/(\rho_{xx}^2 + \rho_{xy}^2)$ and ρ_{xy}^{-1} as a function of V_{tg}. V_{bg} is fixed at 5.16 V. The black solid and dashed lines mark the quantized values of the transverse conductivities. **b**, ρ_{xy}^{-1} as a function of V_{tg}, measured for different V_{bg} values. **c**, Colour map of longitudinal conductivity measured in the filling fraction range of 0–2 and magnetic-field range of 18–34 T at $T = 300$ mK. **d**, Raw data of R_{xx} measured at

different temperatures. **e**, Raw data of ρ_{xy}^{-1} measured at different magnetic fields. V_{bg} is fixed at 5.16 V in **d** and **e**, and data in **a**–**e** are obtained from sample BS10. **f**, Measured gaps Δ of the first three LLs in the range of $B = 10$–14 T in a typical bilayer MoS$_2$ device (sample BS7). The error bars denote the statistical errors in fitting the data using the Arrhenius law.

We now consider the LLs of bilayer MoS$_2$ devices. Their conduction band minima mainly consist of the d_{z^2} electronic orbitals from both layers and are located at the K and K' corners of the Brillouin zone. At these points, the interlayer hybridization carries non-zero orbital angular momentum and cannot couple the rotationally invariant orbitals of opposite layers. The layer index can, therefore, be taken as a good quantum number for electrons in the conduction band. Our calculations (Supplementary Note 1) suggest that a finite vertical electric field E_z can split the layer index in the band structure of LLs, with the first four (lowest and first excited) LLs in the conduction band being layer-valley locked. A calculated band structure of LLs at a layer polarization energy of $E_z = 60$ meV is given in Fig. 2c, with more details of the calculations provided in the Supplementary Information. To visualize the calculated results, the schematic of the first nine LLs (calculated for $B = 40$ T and $E_z = 60$ meV) at the K and K' valleys are illustrated in Fig. 2d, which largely differs from the p-doped scenario observed in monolayer WSe$_2$ (ref. 37).

One key feature of our study is that the Bi/Au electrodes are ohmically contacted with only one top surface of the bilayer MoS$_2$, leading to an asymmetrically contacted configuration. Unlike the monolayer case (Supplementary Fig. 8a), this provides a specific manner to probe the LLs in each of the TMD layers, and enables the observation of LL crossing as shown in the dual-gated scan in Fig. 2e and D–n scan in Supplementary Fig. 8b. When E_z is biased to be sufficiently negative (for example, $D < -0.3$ V nm^{-1} and $n < 5 \times 10^{12}$ cm^{-2}), the system effectively behaves as a monolayer, with the $N = 0$ and $N = 1$ LLs being in the same K valley and on the top layer but carrying opposite spin polarizations. In contrast, when E_z is biased to be less negative or even positive, the lowest LLs generically feature a non-zero amplitude on the bottom layer. Due to the asymmetrically contacted configuration, our measurements only probe a fraction of the total conductivity, leading to interference patterns that perfectly describe the anti-diagonal striped features (Fig. 2e, white dashed lines), as discussed in more detail by

comparing the experimental and simulated results (Supplementary Figs. 11–14).

FQH plateaus in high-quality semiconducting bilayer MoS$_2$

In the following, by applying a vertical magnetic field of up to 34 T at $T = 300$ mK, we examine the QHE in bilayer MoS$_2$ down to the quantum limit of $\nu \leq 1$. Figure 3a displays the $\sigma_{xx} = \rho_{xx}/(\rho_{xx}^2 + \rho_{xy}^2)$ and ρ_{xy}^{-1} as a function of V_{tg}. The quantized plateaus at fractions of 4/5 and 2/5 are observed in the lowest LL, with a clear minima associated in the longitudinal conductance for the former and an emerging one for the latter. This makes semiconducting TMDs another platform to investigate—using electrical transport—FQH states after a few known 2DEG systems of quantum wells and graphene. By varying V_{tg} at different values of fixed V_{bg} (that is, different D values), it is noticed that the FQH states have little dependence on the displacement field in the studied gate-voltage range (Fig. 3b). This hints that—in agreement with earlier arguments—the observed FQH states are layer polarized.

We then focus on the lowest LL with the magnetic field scanned from 34 T down to 18 T (Fig. 3c). Fractionally quantized transverse conductance develops above ~22 T at filling fractions of 4/5 and 2/5, with a clear dip in R_{xx} at 4/5 and an emerging one at 2/5 hidden by a still large (contact) resistivity. Raw data of R_{xx} at different temperatures and ρ_{xy}^{-1} values at different magnetic fields are plotted in Fig. 3d,e, respectively. As a function of temperature, we observe that the kink in R_{xx} at a filling fraction of $\nu = 2/5$ rapidly vanishes near 2 K, and that at $\nu = 4/5$ gradually disappears for T up to 8 K. This means that the FQH gaps are in the order of a few kelvins at 34 T for the typical bilayer MoS$_2$ samples discussed in this work. Meanwhile, the plateaus of ρ_{xy}^{-1} (Fig. 3e) get smeared out below ~26 T, which is the same as that shown in Fig. 3c. It is worth mentioning that the FQH states with a denominator of 5 were reproduced in another typical bilayer MoS$_2$ sample (BS6; Supplementary Fig. 15). We further performed temperature dependence measurements of the quantum oscillations of the LLs (Supplementary Fig. 16), and the gaps of the first three LLs in the range from $B = 10$ T to $B = 14$ T are extracted (Fig. 3f). Indeed, the gap size of the fractionally charged quasiparticles are smaller compared with those estimated at 34 T for integer filling (Fig. 3f).

The FQH state at 4/5 in MoS$_2$ bilayers, which is clearly revealed in our transport measurements, falls in the universality class of the p-h conjugate of Laughlin's 1/5 state[1]. This state hosts Abelian fractionally charged quasiparticles, but differs from the fraction of 1/3, which is usually reported to have the largest gap in Laughlin's hierarchy. Our theoretical calculations show that the $N = 0$ LL in MoS$_2$ bilayers is spanned by radial wavefunctions identical to those observed in standard semiconducting 2DEGs, and experiences a similar Zeeman effect. We, thus, expect similar interacting phases in both systems, including FQH states at 1/3 (or its p-h conjugate 2/3). Deviations from this behaviour most probably come from the non-universal characteristics of the samples, such as disorder, the effective dielectric environment induced by nearby gates or the axial profile of the wavefunctions related to the finite sample thickness.

We were able to theoretically model the latter two, that is, the effects of gates and finite thickness, as a screening of the Coulomb potential at long and short distances, respectively (Methods). In the $N = 0$ LL, this screened Coulomb potential is fully specified by its Haldane pseudopotential V_m, describing the highest energy that two particles with relative angular momentum m can have at the lowest LL (only odd m has an effect on the fermionic states). In Fig. 4a, we plot these pseudopotentials at $B = 22$ T for which the 4/5 fraction appears (Fig. 3c) for an infinitely thin 2DEG, a monolayer MoS$_2$ and a bilayer MoS$_2$ using a realistic gate distance of $d = 35$ nm. The presence of gates yields an exponential decay of V_m at large m, much faster than the standard algebraic decay of the unscreened Coulomb potential. As a result, the few lowest pseudopotentials should already capture the physics of our
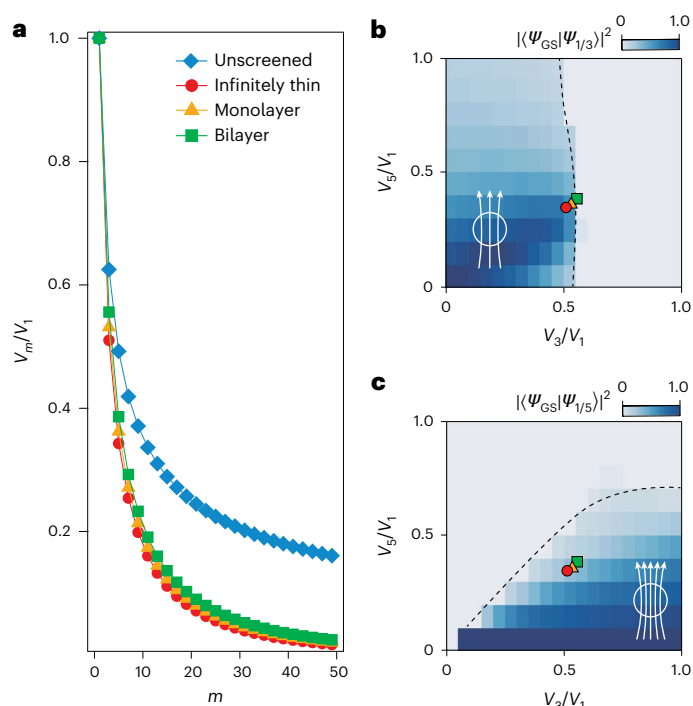

Fig. 4 | Numerical investigation of screening effects. a, Pseudopotential for a gate-screened Coulomb potential in an infinitely thin 2DEG, a monolayer MoS$_2$ and a bilayer MoS$_2$ at $B = 22$ T and a gate distance of $d = 35$ nm (Methods). V_m is the Haldane pseudopotential that describes the maximum energy that two particles with relative angular momentum m can have at the lowest LL. We show the pseudopotentials of an unscreened Coulomb potential for comparison. **b**, Square overlap between the exact diagonalization ground state $|\Psi_{GS}\rangle$ and Laughlin's wavefunction $|\Psi_{1/3}\rangle$ numerically computed on a torus with $N = 13$ electrons at a filling fraction of 1/3 using three non-zero pseudopotentials $V_{m=1,3,5}$. The coloured dots show the values extracted from **a**. **c**, Same data as **b**, but at a filling fraction of 1/5 using $N = 10$ particles. The cartoons in **b** and **c** illustrate the Laughlin phases of 1/3 and 1/5, respectively, with the black dashed lines highlighting the boundary between a Laughlin-like phase (non-zero overlaps, that is, the blue-coloured area) and a phase in which the Laughlin state is absent (vanishing overlaps, that is, the white-coloured area).

gate-screened samples, and we restrict our attention to the first three ones, namely, V_1, V_3 and V_5, hereafter.

Figure 4a also points out that the finite thickness of the sample increases $V_{m>1}$ compared with V_1. Due to their exact clustering properties, FQH states are sensitive to such changes in the short-range interaction physics. For instance, the ground state of an FQH system at a filling of 1/3 has perfect overlap with the Laughlin state when $V_1 > 0$ and all $V_{m>1} = 0$, but this overlap decreases as V_3 and V_5 grow[50] (in Fig. 4b, we plot this overlap obtained for a finite torus using exact diagonalization (Methods)). For $V_3 \gtrsim 0.5V_1$, this overlap vanishes, signalling a phase transition and a ground state that no longer belongs to the Laughlin universality class. The increase in $V_{m>1}/V_1$ in bilayer MoS$_2$ (Fig. 4a) drives the system to the edge of the phase that has non-zero overlap with Laughlin's 1/3 state, hinting at a potential absence of the FQH state at 2/3 in our experiments. Consistent with our experiments, the same calculation at a filling of 1/5 (Fig. 4c) shows that the stability of fractions 1/5, or its p-h conjugate 4/5, barely changes as we go from an infinitely thin 2DEG to a realistic bilayer MoS$_2$. In conclusion, although all the microscopic details of our samples are not necessarily captured by our calculations, they reveal a clear trend that rationalizes the absence of the 2/3 FQH state due to the internal screening of the Coulomb potential. It is noticed that for the typical monolayer MoS$_2$ devices, Laughlin's 1/3 states are also absent, though the hints of FQH states in monolayer samples exhibit less well-defined quantization at a filling

of 1/5 compared with the bilayer ones (Supplementary Fig. 17). The 2/5 and 1/3 FQH states belong to the same series, and are stabilized by a similar pseudopotential sequence (the overlap square between the ground state for the Coulomb interaction and the V_1–V_3–V_5 pseudopotentials at a filling of 2/5 is shown in Supplementary Fig. 18). We would, therefore, expect that the 2/5 state is less stable in the presence of dielectric screening. As hinted by the breaking of the p-h symmetry between 2/5 and 3/5 (Fig. 3), the effects of spin degeneracy might be important at these fractions. The observed sensitivity of the FQH states to the dielectric environment imposed by nearby gates and by the vertical profile of the heterostructure may allow the engineering of a richer phenomenology of FQH states in TMD-based heterostructures[51]. Recently, transport evidence of FQH states in p-type WSe$_2$ has also been reported[52].

Conclusions

We have reported ohmic contacts to n-type bilayer MoS$_2$ with an extremely low carrier density. We measured the electrical transport characteristics under high magnetic fields of up to 34 T and a base temperature of 300 mK. Our device fabrication technique leads to field-effect mobilities of over 100,000 cm^2 V^{-1} s^{-1} and quantum mobilities of over 3,000 cm^2 V^{-1} s^{-1} in the conduction band in monolayer MoS$_2$ at millikelvin temperatures. Under the application of finite E_z, the system behaves as a monolayer MoS$_2$ whose first four LLs in the conduction band are layer-valley locked, and the spin degeneracy is fully lifted by the Zeeman shift. The asymmetric ohmic contact to the high-mobility bilayer semiconducting channel leads to the observation of fractionally quantized Hall plateaus of 2/5 and 4/5 in the lowest LL above 26 T, which exhibit negligible tunability against E_z, and are at the energy scale of sub-1 K, in agreement with theoretical predictions. The high mobility in our devices could potentially lead to TMD twistronics, Coulomb drag devices and low-temperature high-electron-mobility transistors. Our work could also help in the development of low-density transport experiments on TMD heterostructures, which will be required to harness the full potential of topological FQH phases[53–56].

Methods

Sample fabrication

van der Waals few layers of the hBN/MoS$_2$/hBN sandwich were obtained by mechanically exfoliating high-quality bulk crystals. The vertical assembly of the van der Waals layered compounds were fabricated by using the dry-transfer method in a nitrogen-filled glove box. Hall bars of hBN/MoS$_2$/hBN devices were achieved by plasma etching. Electron-beam lithography was performed using a ZEISS Sigma 300 scanning electron microscope with a Raith Elphy Quantum graphic writer. The top gates and contacting electrodes were fabricated with a thermal evaporator, with typical Bi/Au thicknesses of ~25/30 nm.

High-magnetic-field facilities

A resistive magnet with a maximum magnetic field of 34 T and a base temperature of 300 mK was used. The facility was equipped with a water cooling system, and is maintained by the Steady High Magnetic Field Facility, High Magnetic Field Laboratory, Chinese Academy of Sciences.

Electrical measurements

The high precision of the current measurements of the devices were achieved using a Cascade M150 probe station at room temperature, with an Agilent B1500A semiconductor device parameter analyser. The gate voltages on the as-prepared Hall bars were maintained by a Keithley 2400 source meter. During the measurements, the TMD layer was fed with an a.c. I_{bias} of about 10 nA. Low-frequency lock-in four-probe measurements were used throughout the transport measurements under a high magnetic field and at low temperatures.

Theoretical modelling

The LL diagrams for monolayer and bilayer MoS$_2$ are obtained by applying minimal coupling on the $\vec{k} \cdot \vec{p}$ Hamiltonian for conduction electrons derived from ab initio simulations. The calculation follows from another formalism[57], which is reviewed in the Supplementary Information for completeness. We use values of the gap, effective mass, Ising spin–orbit coupling strength in the conduction and valence bands, spin and valley g-factors, and uniform interlayer hybridization provided by first-principles calculations[58,59] and rounded off to the millielectron-volt scale.

To describe the interacting phases of our system, we have used the Coulomb potential $V(q) = 2\pi e^2 \tanh(qd)/[\varepsilon q(1 + n\alpha q\delta)]$, which faithfully captures the long-distance (small-q) and short-distance (large-q) asymptotics imposed by gate screening and the out-of-plane structure of MoS$_2$ multilayers, respectively. More precisely, this Coulomb potential reproduces (1) $V(q\to 0) = 2\pi e^2 \tanh(qd)/(\varepsilon q)$ expected in the presence of gates symmetrically placed at a distance d around the sample, where $\varepsilon \simeq 5$ is the relative dielectric constant of the surrounding hBN; and (2) a Rytova–Keldysh form $V(q\to\infty) = 2\pi e^2/[\varepsilon q(1 + n\alpha q\delta)]$ known to be relevant for TMDs[60], where n is the number of layers, $\delta = 0.65$ nm is the typical interlayer spacing and α is a material-specific constant. Note that $n = 0$ describes an infinitely thin 2DEG with no short-range screening.

Interactions projected to the $N = 0$ LL are accounted for by using Haldane's pseudopotentials[61], defined on the plane as $V_m = (2\pi\ell_B^2)^{-1} \int_0^\infty \tilde{q} d\tilde{q} V(\tilde{q}/\ell_B) L_m(\tilde{q}^2) e^{-\tilde{q}^2}$, where ℓ_B is the magnetic length, L_m is the mth Laguerre polynomial and $V(q)$ is the Coulomb potential. This should be understood as an angular Fourier transformation of the Coulomb potential after projection to the $N = 0$ LL, such that V_m energetically penalizes particles with relative angular momentum m. Note that fermions are only sensitive to odd-m pseudopotentials. The FQH state at a fraction of 4/5 is observed in the magnetic-field range of 22–34 T, for which the magnetic length lies within $\ell_B \simeq 4.5$–6 nm. Focusing on $B = 22$ T (Fig. 4a), the ~35-nm-thick boron nitride layers between our sample and gates yields $d/\ell_B \simeq 6$, whereas the coefficient $\alpha = 15/\varepsilon$ (ref. 62) leads to $\alpha\delta/\ell_B \simeq 0.4$. Both these estimates have been rounded to their first significant digit to highlight their phenomenological nature.

The phase diagrams shown in Fig. 4b,c were obtained by the exact numerical diagonalization of the interacting problem on the torus with a square aspect ratio including the three first potentials relevant for fermions, namely, V_1, V_3 and V_5. We set $V_1 = 1$ to fix the energy scale. The Hilbert-space dimensions for $N = 13$ particles at a filling of 1/3 and $N = 10$ particles at a filling of 1/5 are 16,020,564 and 20,544,878, respectively, in the momentum sectors of their ground state.

Data availability

The data that support the findings of this study are available via Zenodo at https://doi.org/10.5281/zenodo.13765107 (ref. 63).

Code availability

The exact diagonalization results were obtained using DiagHam, an open-source publicly available software package available at https://www.nick-ux.org/diagham.

References

1. Laughlin, R. B. Anomalous quantum Hall effect: an incompressible quantum fluid with fractionally charged excitations. *Phys. Rev. Lett.* **50**, 1395–1398 (1983).
2. Eisenstein, J. P. & Stormer, H. L. The fractional quantum Hall effect. *Science* **248**, 1510–1516 (1990).
3. Stormer, H. L., Tsui, D. C. & Gossard, A. C. The fractional quantum Hall effect. *Rev. Mod. Phys.* **71**, S298 (1999).
4. Feldman, D. E. & Halperin, B. I. Fractional charge and fractional statistics in the quantum Hall effects. *Rep. Prog. Phys.* **84**, 076501 (2021).

5. Jain, J. K. Composite-fermion approach for the fractional quantum Hall effect. *Phys. Rev. Lett.* **63**, 199 (1989).

6. Pan, W. et al. Fractional quantum Hall effect of composite fermions. *Phys. Rev. Lett.* **90**, 016801 (2003).

7. Son, D. T. The Dirac composite fermion of the fractional quantum Hall effect. *Annu. Rev. Condens. Matter Phys.* **9**, 397–411 (2018).

8. Moore, G. & Read, N. Nonabelions in the fractional quantum Hall effect. *Nucl. Phys. B* **360**, 362–396 (1991).

9. Stern, A. Anyons and the quantum Hall effect—a pedagogical review. *Ann. Phys.* **323**, 204–249 (2008).

10. Lin, X., Du, R. & Xie, X. Recent experimental progress of fractional quantum Hall effect: 5/2 filling state and graphene. *Natl Sci. Rev.* **1**, 564–579 (2014).

11. Clarke, D. J., Alicea, J. & Shtengel, K. Exotic non-abelian anyons from conventional fractional quantum Hall states. *Nat. Commun.* **4**, 1348 (2013).

12. Vaezi, A. Superconducting analogue of the parafermion fractional quantum Hall states. *Phys. Rev. X* **4**, 031009 (2014).

13. Alicea, J. & Fendley, P. Topological phases with parafermions: theory and blueprints. *Annu. Rev. Condens. Matter Phys.* **7**, 119–139 (2016).

14. Tsui, D. C., Stormer, H. L. & Gossard, A. C. Two-dimensional magnetotransport in the extreme quantum limit. *Phys. Rev. Lett.* **48**, 1559 (1982).

15. Tsukazaki, A. et al. Observation of the fractional quantum Hall effect in an oxide. *Nat. Mater.* **9**, 889–893 (2010).

16. Falson, J. & Kawasaki, M. A review of the quantum Hall effects in MgZnO/ZnO heterostructures. *Rep. Prog. Phys.* **81**, 056501 (2018).

17. Du, X., Skachko, I., Duerr, F., Luican, A. & Andrei, E. Y. Fractional quantum Hall effect and insulating phase of Dirac electrons in graphene. *Nature* **462**, 192–195 (2009).

18. Dean, C. R. et al. Multicomponent fractional quantum Hall effect in graphene. *Nat. Phys.* **7**, 693–696 (2011).

19. Feldman, B. E., Krauss, B., Smet, J. H. & Yacoby, A. Unconventional sequence of fractional quantum Hall states in suspended graphene. *Science* **337**, 1196 (2012).

20. Maher, P. Tunable fractional quantum Hall phases in bilayer graphene. *Science* **345**, 61–64 (2014).

21. Kou, A. et al. Electron-hole asymmetric integer and fractional quantum Hall effect in bilayer graphene. *Science* **345**, 55–57 (2014).

22. Amet, F. et al. Composite fermions and broken symmetries in graphene. *Nat. Commun.* **6**, 5838 (2014).

23. Li, J. I. A. et al. Even denominator fractional quantum Hall states in bilayer graphene. *Science* **358**, 648–652 (2017).

24. Zibrov, A. A. et al. Tunable interacting composite fermion phases in a half-filled bilayer-graphene Landau level. *Nature* **549**, 360–364 (2017).

25. Kim, Y. et al. Even denominator fractional quantum Hall states in higher landau levels of graphene. *Nat. Phys* **15**, 154–158 (2019).

26. Zibrov, A. A. et al. Even-denominator fractional quantum Hall states at an isospin transition in monolayer graphene. *Nat. Phys.* **14**, 930–935 (2018).

27. Huang, K. et al. Valley isospin controlled fractional quantum Hall states in bilayer graphene. *Phys. Rev. X* **12**, 031019 (2022).

28. Li, X., Zhang, F. & Niu, Q. Unconventional quantum Hall effect and tunable spin Hall effect in Dirac materials: application to an isolated MoS_2 trilayer. *Phys. Rev. Lett.* **110**, 066803 (2013).

29. Pisoni, R. et al. Interactions and magnetotransport through spin-valley coupled Landau levels in monolayer MoS_2. *Phys. Rev. Lett.* **121**, 247701 (2018).

30. Lin, J. et al. Determining interaction enhanced valley susceptibility in spin-valley-locked MoS_2. *Nano Lett.* **19**, 1736–1742 (2019).

31. Xu, S. et al. Odd-integer quantum Hall states and giant spin susceptibility in p-type few-layer WSe_2. *Phys. Rev. Lett.* **118**, 067702 (2017).

32. Wang, Z., Shan, J. & Mak, K. F. Valley- and spin-polarized Landau levels in monolayer WSe_2. *Nat. Nanotechnol.* **12**, 144–149 (2017).

33. Movva, H. C. P. et al. Density-dependent quantum Hall states and Zeeman splitting in monolayer and bilayer WSe_2. *Phys. Rev. Lett.* **118**, 247701 (2017).

34. Wu, Z. et al. Even-odd layer-dependent magnetotransport of high-mobility Q-valley electrons in transition metal disulfides. *Nat. Commun.* **7**, 12955 (2016).

35. Gustafsson, M. V. et al. Ambipolar Landau levels and strong band-selective carrier interactions in monolayer WSe_2. *Nat. Mater.* **17**, 411–415 (2018).

36. Masseroni, M. et al. Electron transport in dual-gated three-layer MoS_2. *Phys. Rev. Res.* **3**, 023047 (2021).

37. Shi, Q. et al. Odd- and even-denominator fractional quantum Hall states in monolayer WSe_2. *Nat. Nanotechnol.* **15**, 569–573 (2020).

38. Kappera, R. et al. Phase-engineered low-resistance contacts for ultrathin MoS_2 transistors. *Nat. Mater.* **13**, 1128–1134 (2014).

39. Cai, X. et al. Bridging the gap between atomically thin semiconductors and metal leads. *Nat. Commun.* **13**, 1777 (2022).

40. Yuan Liu, Y. et al. Approaching the Schottky-Mott limit in van der Waals metal-semiconductor junctions. *Nature* **557**, 696–700 (2018).

41. Li, W. et al. Approaching the quantum limit in two-dimensional semiconductor contacts. *Nature* **613**, 274–279 (2023).

42. Shen, P.-C. et al. Ultralow contact resistance between semimetal and monolayer semiconductors. *Nature* **593**, 211–217 (2021).

43. Wang, L. et al. One-dimensional electrical contact to a two-dimensional material. *Science* **342**, 614–617 (2013).

44. Jung, Y. et al. Transferred via contacts as a platform for ideal two-dimensional transistors. *Nat. Electron.* **2**, 187–194 (2019).

45. Pisoni, R. et al. Absence of interlayer tunnel coupling of K-valley electrons in bilayer MoS_2. *Phys. Rev. Lett.* **123**, 117702 (2019).

46. Chuang, H.-J. et al. Low-resistance 2D/2D ohmic contacts: a universal approach to high-performance WSe_2, MoS_2, and $MoSe_2$ transistors. *Nano Lett.* **16**, 1896–1902 (2016).

47. Movva, H. C. et al. High-mobility holes in dual-gated WSe_2 field-effect transistors. *ACS Nano* **9**, 10402–10410 (2015).

48. Chuang, H.-J. et al. High mobility WSe_2 p- and n-type field-effect transistors contacted by highly doped graphene for low-resistance contacts. *Nano Lett.* **14**, 3594–3601 (2014).

49. Cui, X. et al. Low-temperature ohmic contact to monolayer MoS_2 by van der Waals bonded Co/h-BN electrodes. *Nano Lett.* **17**, 4781–4786 (2017).

50. Regnault, N. et al. Evidence of a fractional quantum Hall nematic phase in a microscopic model. *Phys. Rev. B* **96**, 035150 (2017).

51. Papić, Z. et al. Numerical studies of the fractional quantum Hall effect in systems with tunable interactions. *J. Phys.: Conf. Ser.* **402**, 012020 (2012).

52. Pack, J. et al. Charge-transfer contacts for the measurement of correlated states in high-mobility WSe_2. *Nat. Nanotechnol.* **19**, 948–954 (2024).

53. Cai, J. et al. Signatures of fractional quantum anomalous Hall states in twisted $MoTe_2$. *Nature* **622**, 63–68 (2023).

54. Zeng, Y. et al. Thermodynamic evidence of fractional Chern insulator in moiré $MoTe_2$. *Nature* **622**, 69–73 (2023).

55. Park, H. et al. Observation of fractionally quantized anomalous Hall effect. *Nature* **622**, 74–79 (2023).

56. Xu, F. et al. Observation of integer and fractional quantum anomalous Hall effects in twisted bilayer $MoTe_2$. *Phys. Rev. X* **13**, 031037 (2023).

57. Zubair, M. et al. Quantum magnetotransport in bilayer MoS$_2$: influence of perpendicular electric field. *Phys. Rev. B* **96**, 045405 (2017).

58. Kormányos, A. et al. Spin-orbit coupling, quantum dots, and qubits in monolayer transition metal dichalcogenides. *Phys. Rev. X* **4**, 011034 (2014).

59. Fang, S. et al. Ab initio tight-binding Hamiltonian for transition metal dichalcogenides. *Phys. Rev. B* **92**, 205108 (2015).

60. Meckbach, L. et al. Influence of the effective layer thickness on the ground-state and excitonic properties of transition-metal dichalcogenide systems. *Phys. Rev. B* **97**, 035425 (2018).

61. Girvin, S. M. The quantum Hall effect: novel excitations and broken symmetries. In *Aspects topologiques de la physique en basse dimension* 53–175 (Springer, 2002).

62. Van Tuan, D. et al. Coulomb interaction in monolayer transition-metal dichalcogenides. *Phys. Rev. B* **98**, 125308 (2018).

63. Zhao, S. Fractional quantum Hall phases in high mobility n-type molybdenum disulfide transistors. *Zenodo* https://doi.org/10.5281/zenodo.13765107 (2024).

64. Ma, N. & Jena, D. Charge scattering and mobility in atomically thin semiconductors. *Phys. Rev. X* **4**, 011043 (2014).

Acknowledgements

Author contributions

Competing interests

The authors declare no competing interests.

Additional information

¹Liaoning Academy of Materials, Shenyang, China. ²Shenyang National Laboratory for Materials Science, Institute of Metal Research, Chinese Academy of Sciences, Shenyang, China. ³School of Material Science and Engineering, University of Science and Technology of China, Anhui, China. ⁴Center for Computational Quantum Physics, Flatiron Institute, New York, NY, USA. ⁵State Key Laboratory of Quantum Optics and Quantum Optics Devices, Institute of Optoelectronics, Shanxi University, Taiyuan, China. ⁶Collaborative Innovation Center of Extreme Optics, Shanxi University, Taiyuan, China. ⁷State Key Laboratory for Mesoscopic Physics, School of Physics, Peking University, Beijing, China. ⁸Anhui Key Laboratory of Low-Energy Quantum Materials and Devices, High Magnetic Field Laboratory, HFIPS, Chinese Academy of Sciences, Hefei, China. ⁹Beijing National Laboratory for Condensed Matter Physics and Institute of Physics, Chinese Academy of Sciences, Beijing, China. ¹⁰School of Physical Sciences, University of Chinese Academy of Sciences, Beijing, China. ¹¹Research Center for Electronic and Optical Materials, National Institute for Materials Science, Tsukuba, Japan. ¹²Research Center for Materials Nanoarchitectonics, National Institute for Materials Science, Tsukuba, Japan. ¹³Université Grenoble Alpes, CNRS, Grenoble INP, Institut Néel, Grenoble, France. ¹⁴Department of Physics and the Center for 1D/2D Quantum Materials, the Hong Kong University of Science and Technology, Hong Kong, China. ¹⁵Laboratoire de Physique de L'Ecole normale supérieure, ENS, Université PSL, CNRS, Sorbonne Université, Université Paris-Diderot, Paris, France. ¹⁶Department of Physics, Columbia University, New York, NY, USA. ¹⁷These authors contributed equally: Siwen Zhao, Jinqiang Huang, Valentin Crépel. ✉e-mail: jzhang74@sxu.edu.cn; phwang@ust.hk; jmlu@pku.edu.cn; nicolas.regnault@phys.ens.fr; vitto.han@gmail.com